4

Trichromatic High Resolution-LBIC: A System for the Micrometric Characterization of Solar Cells

Javier Navas, Rodrigo Alcántara, Concha Fernández-Lorenzo and Joaquín Martín-Calleja
University of Cádiz
Spain

1. Introduction

Laser Beam Induced Current (LBIC) imaging is a nondestructive characterization technique which can be used for research into semiconductor and photovoltaic devices (Dimassi et al., 2008). Since its first application to p-n junction photodiode structures used in HgCdTe infrared focal plane arrays in the late 1980s, many experimental studies have demonstrated the LBIC technique's capacity to electrically map active regions in semiconductors, as it enables defects and details to be observed which are unobservable with an optical microscope (van Dyk et al., 2007). Thus, the LBIC technique has been used for research in different fields related to photovoltaic energy: the superficial study of silicon structures (Sontag et al. 2002); the study of grain boundaries on silicon based solar cells (Nishioka et al., 2007); the study of polycrystalline solar cells (Nichiporuk et al., 2006); the study of thin film photovoltaic modules (Vorasayan et al., 2009); the study of non-silicon based photovoltaic or semiconductor devices (van Dyk et al., 2007) and the study of dye-sensitized solar cells (Navas et al., 2009).

In this technique, a highly stabilized laser beam is focused on the photoactive surface of a cell and performs a two-dimensional scan of the photoactive surface, measuring the photoresponse generated point to point. A correlation between the number of incident photons and the quantity of photoelectrons generated derived from the photocurrent measurement makes it possible to obtain the photoconverter efficiency, which is the quantum efficiency of the device at each point of the active surface. Thus, the LBIC technique allows images of photovoltaic devices to be obtained dependent upon superficial variation in quantum efficiency. Usually photocurrent values are measured at short circuit as it is a linear function of the radiation power in a wide range and the interaction coefficient is proportional to the quantum photoefficiency (Bisconti et al., 1997). Three main factors can be associated to the level of photocurrent generated by a photovoltaic surface: (a) the limit values of photon energy that are necessary for electron transfer between valence and conduction bands, (b) the intrinsic characteristics of electron-hole recombination, and (c) photon penetration into the active material.

So, the numerical value of the photoefficiency signal generated at each point is computer stored according to its positional coordinates. Using the stored signal, an image is generated

of the photoconversion efficiency of the surface scanned. It is interesting to note that the whole photoactive surface acts as an integrating system. That is, independent of the irradiated area or its position, the entire photogenerated signal is always obtained via the system's two connectors.

The spatial resolution of the images obtained depends on the size of the laser spot. That is, images generated using the LBIC technique have the best possible resolution when the focusing of the beam on the cell is optimum. Thus, it is essential to use a laser as the irradiation system because it provides optimal focusing of the photon beam on the photoactive surface and therefore a higher degree of spatial resolution in the images obtained. This provides enhanced structural detail of the material at a micrometric level which can be related with the quantum yield of the photovoltaic device. However, the monochromatic nature of lasers means that it is impossible to obtain information about the response of the device under solar irradiation conditions. No real irradiation source can simultaneously provide a spectral distribution similar to the emission of the sun with the characteristics of a laser emission in terms of non divergence and Gaussian power distribution.

Nowadays, there are several LBIC systems with different configurations which have been developed by research groups and allowing interesting results to be obtained (Bisconti et al., 1997). In general, these systems are based on a laser source which, by using different optomechanical systems to prepare the radiation beam, is directed at a system which focalizes it on the active surface of the device. There are two options for performing a superficial scan in low spatial resolution systems: using a beam deflection technique or placing the photovoltaic device on a biaxial displacement system which positions the photoactive surface in the right position for each measurement. The system must incorporate the right electrical contacts, as well as the necessary electronic systems, to gather the photocurrent signal and prepare it to be measured so that an image can be created which is related with the quantum efficiency of the device under study. However, high resolution (HR) spatial systems (HR-LBIC) must use a very short focal distance focusing lens, which prevents deflection systems being used to perform the scan and makes it necessary to opt for systems with biaxial displacement along the photoactive surface.

2. LBIC system description

The different components which make up the subsystems of the equipment, such as the elements used for focusing the beam on the active surface, controlling the radiant power, controlling the reflected radiant power, etc., are placed along the optical axis (see Figure 1).

In our system we have used the following as excitation radiation emissions: a 632.8 nm He–Ne laser made by Uniphase ©, model 1125, with a nominal power of 10 mW; a 532 nm DPSS laser made by Shangai Dream Lasers Technology ©, model SDL-532–150T, with a nominal power of 150 mW; and a 473 nm DPSS laser by Shangai Dream Lasers Technology©, model SDL-473–040T, with a nominal power of 40 mW. Each of the lasers is mounted on a system allowing optimal adjustment of the optical pathway, with a predetermined angle between them. In turn, a shutter is placed in the optical pathway of each laser which makes it possible to establish the radiation used in each scan. In order to reduce the laser power to the required values, a continuous neutral density filter is placed next the laser exit windows. The layout of the three lasers enables their beams to come together on a mirror supported on a stepper motor, which being set at a predefined angle makes it possible to direct the

radiation from the selected laser through the whole system's main optical pathway. A Micos SMC Pollux stepper motor controller with an integrated two-phase stepper motor, capable of moving 1.8°/0.9° per step has been used for motor control. Command programming and configuration is executed via a RS232 interface, which allows velocity movement definition, point to point moves, and multiple unit control with only one communication port.

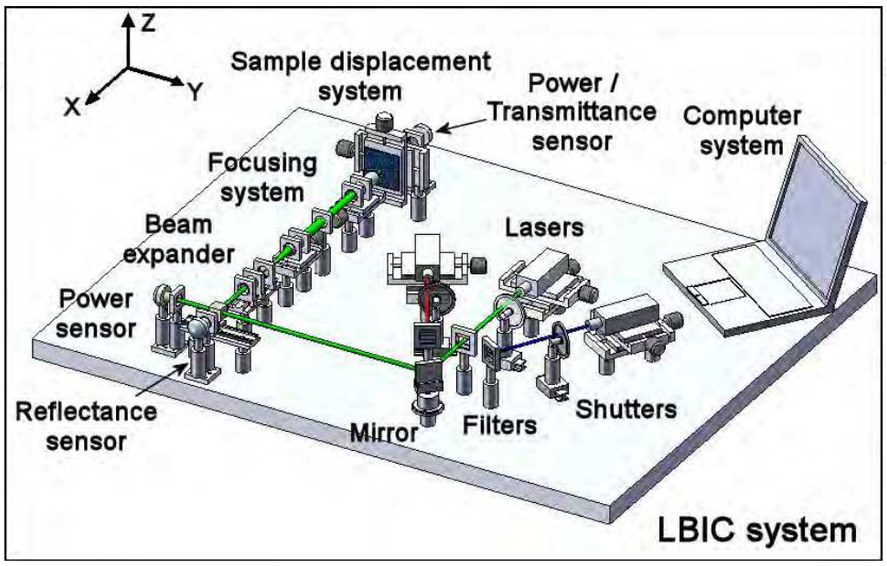

Fig. 1. General outline of the LBIC system.

A highly transparent nonpolarizing beamsplitter, made from BK7 glass with antireflecting coating, has been placed on the optical path. This beamsplitter plays a double role, depending on whether it is working in reflection or in transmission. In reflection, the reflected beam is used for irradiating the sample, whereas the transmitted beam allows one to monitor the stability of the laser power emission by using a silicon photodiode (see Figure 1). By means of the ratio between the induced current and this signal it is possible to obtain a normalized value for the external quantum efficiency.

The optical system between the beamsplitter and the sample works similarly to a confocal system, so that the beam specularly reflected by the sample surface follows an optical path which coincides with the irradiation path, but in the opposite sense. The intensity of this beam that is reflected by beam splitter is measured by a second silicon photodiode which allows one to obtain information on the reflecting properties of the photoactive surface. This information is particularly interesting for the evaluation of the photoconversion internal quantum efficiency. Moreover, when the photovoltaic device under study has a photon transparent support as in dye-sensitized solar cells, the transmittance signal can also be measured (see Figure 1).

This system is most important since an optimum focusing of the laser on the photoactive surface is one of the main limiting factors of the spatial resolution. Any focusing errors will lead to unacceptable results. The focusing system designed consists basically of three subsystems: a focusing lens mounted on a motorized stage with micrometric movement, a beam expander built with two opposing microscope objectives and a calculation algorithm which allows a computer to optimize the focusing process, and which we will analyze in detail later. The spot size at the focus is directly related to the focal distance and inversely

related to the size of the prefocused beam. In this case, the focusing lenses we have used were, either a 16x microscope objective (F:11 mm) or a 10x one (F:15.7 mm), both supplied by Owis GMBH. The beam emitted by the lasers we previously mentioned has a size of 0.81 mm in the TEM_{00} mode, and it has been enlarged up to 7.6 mm by means a beam expander made up of two microscope objectives, coaxially and confocally arranged, with a 63x:4x rate. In order to eliminate as many parasitic emissions as possible, a spatial filter is placed at the confocal point of expander system and the resulting emission of the system is diaphragmed to the indicated nominal diameter (7.6 mm). Focusing with objectives of different magnification values will produce different beam parameters at the focus, affecting the resolution capacity to which photoactive surfaces can be studied.
We have decided to use a system configuration consisting of a fixed beam and mobile sample moving along orthogonal directions (YZ plane) with respect to the irradiation optical axis. The biaxial movement of the photoactive surface is achieved by using a system of motorized stages with numerical control and displacement resolution of 0.5 μm. Special care has been taken to ensure the minimization of the asymmetrically suspended masses so as to avoid the generation of gravitational torsional forces. All optomechanical elements utilized in this system have been provided by Owis GMBH. Moreover, two low ohmic electric contacts are used to extract the electrons generated.

3. Focusing algorithm

A TEM_{00} mode laser beam presents a Gaussian irradiance distribution. This distribution is not modified by the focusing or reflecting of the beam by means of spherical optical elements and the irradiance is calculated by means of the expression

$$I(r)=I_0 \cdot \exp\left(-\frac{2r^2}{w^2}\right), \tag{1}$$

where r is the distance from the center of the optical axis and w the so-called Gaussian radius, defined as the distance from the optical axis to the position at which the intensity decreases to $1/e^2$ of the value on the optical axis.
When a monochromatic Gaussian beam is focused, the Gaussian radius in the area near the focus fits the equation

$$w^2(x)=w_0^2\left[1+\left(\frac{\lambda x}{\pi n w_0^2}\right)^2\right], \tag{2}$$

where x is the coordinate along the propagation axis with the origin of coordinates being defined at the focal point, λ the wavelength value, n the refraction index of the medium and w_0 is the Gaussian radius value at the focus. The latter can be obtained from the expression

$$w_0=\left(\frac{2\lambda}{\pi}\right)\left(\frac{F}{D}\right), \tag{3}$$

where F is the focal distance of the lens and D is the Gaussian diameter of the prefocused beam.
For a monochromatic beam, the energy irradiance is proportional to the photon irradiance. As we explained above, in an ideal focusing process, the beam power remains constant, which implies that the number of photons is also kept constant. Assuming that (a) only the photons absorbed can generate electron–hole pairs according to a given quantum yield, (b)

there are no biphotonic processes in normal conditions and (c) the power is low enough as to ignore thermal effects, then we can say that the intensity of the current supplied by the cell must be proportional to the density of incident photons and to the photoconversion efficiency of the cell. This implies that for an ideally homogeneous photoconversion surface, the current intensity generated will be independent of the focusing level, since, except when the size of the beam is larger than the active surface, the total number of photons will be a constant independent of its focusing level. In such a case the measure of current intensity would not be used to judge whether the laser beam is optimally focused.

The situation is quite different if the photoconversion surface has heterogeneities. In that case, the size of the heterogeneity would match the size of the photon beam. The definition of heterogeneity would depend on the type of cell we are working with. In monocrystalline solar cells we may consider the cell's edges or the electron-collecting conducting elements (fingers); in polycrystalline solar cells, in addition to the previously mentioned ones, we may also consider the grain boundaries, the dislocations or any other photoconversion defects and, in dye sensitized solar cells, porous semiconductors density irregularities, dye adsorption concentration, etc. The current I_{SC} generated will depend on the illuminated surface quantum yield average value, which, at the same time is dependant of the spot size and the distribution power. This dependence can be used to optimally focus the laser beam on the active surface.

The basic experimental set-up has been defined before (see Figure 1). According to this diagram, the solar cell or photoelectrical active surface is placed on the YZ plane. Orthogonal to this surface and placed along the X-axis, a laser beam falls on. This laser is focused by a microscope objective lens, which can travel along that axis by means of a computer-controlled motorized stage. In turn, the solar cell is fixed to two motorized stages which allow it to move on the YZ plane, along a coordinate named l so that

$$\Delta l=\sqrt{\Delta y^2+\Delta z^2}\ . \tag{4}$$

For every position along the l coordinate, a value for the short circuit current is obtained (I_{SC}) that is proportional to its quantum efficiency. The graphic representation of $I_{SC}(l)$ versus l gives rise to the so-called I_{SC}-curve.

In order to analyze the I_{SC}-curve, it is assumed that the photoactive surface is equivalent to an independent set of photoconversion spatial pixels, each one having individual quantum efficiencies in the 0–100% range. These quantum efficiencies can be individually measured only if the size of the laser beam used as probe is equal or lesser than the aforementioned spatial pixels. If the laser beam spot is greater than these basic units, the electric response obtained will be equivalent to the product of the quantum efficiency distribution values of the affected units multiplied by the laser beam geometry photonic intensity.

Figure 2A shows an example of an I_{SC}-curve. This one was obtained after performing a scan through a metallic current collector on a Silicon monocrystalline (mc-Si) solar cell. In this case, the laser beam has been focused by means of a 10x microscope objective lens, generating a minimum spot (w_0) on the order of 1.2 μm in diameter. Initially, the whole laser spot falls on a high photoconversion efficiency surface, generating a high I_{SC} value, showing small variations caused by little heterogeneities (zone 1), later, when the laser starts to intercept the finger, a gradual I_{SC} decreasing is generated (zone 2). If the collector width is greater than the laser spot diameter, the laser beam must travel through an area in which only a minimum current, associated to the diffuse light, is generated (zone 3). Subsequently the spot will gradually fall again on the photoactive sector (zone 4) until the spot again fully

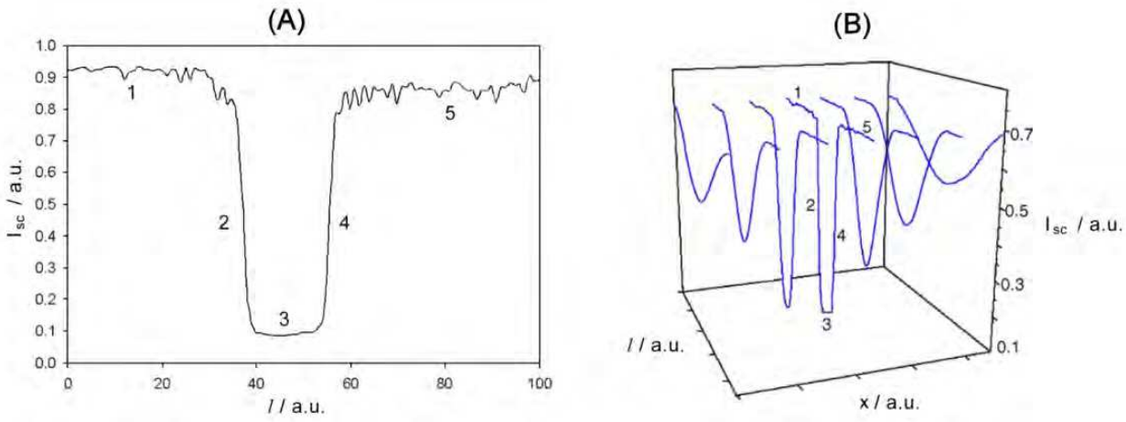

Fig. 2. (A) I_{SC}-curve obtained after performing a linear scan along a l superficial coordinate on a Si(MC) solar cell and through a current collector. (B) I_{SC}-curve generated at different positions of the focal lens along X-axis.

falls on the high efficiency photoactive surface (zone 5). When the laser is not perfectly focused, the spot size diameter on the surface is larger than w_0 and the same scan through the metallic collector generates an I_{SC}-curve where signal measured at each position is a mean value of a wide zone. This generates a softer transition between regions with abrupt changes of their quantum efficiencies. In other words, the smaller the spot size, the more abrupt the I_{SC} transition between zones with different superficial photoactivity due to the different photoconversion units are better detected. Figure 2B shows the aforementioned variations of the I_{SC}-curve according to the focal lens position. The I_{SC}-curve in the center of the figure (numbered as 3) corresponds to that one appearing in Figure 2A, that is, the curve generated when the focal lens is in the optimum focusing position, i.e. the smallest spot size.

3.1 Scan methodologies

In order to obtain a data set with information about the optimum focusing position two experimental methodologies can be used. The first one, so called EM1, involves performing successive linear scans along a l coordinate on the photoactive surface, from different x_f focal lens positions. This methodology will lead us to an EM1(I_l, x_f) matrix, whose graphic representation by scan vectors is similar than the one shown in Figure 3B. The second methodology, called EM2, is a particular case of the first one and involves synchronizing the displacement along the l coordinate with the focal lens displacement along the x coordinate. Then, only a vector data set is obtained and it is equivalent to the main diagonal of the aforementioned data EM1(I_l, x_f) matrix, so a substantial reduction in the number of experimental points is achieved. In this case, the evaluation of the EM2(x_f) data vector is carried out by defining several data subsets of n points of length, ranging from the first point to the total number of points minus n. So, to analyze the previously defined data set, the numerical analysis using derivative function has been used. The purpose is to generate a new data set with a singular point associated to the optimum focusing position. This new data set is named Focal-curve. With this aim, the I_{SC}-curve data set properties must be numerically evaluated.

3.2 Focal-curve: Derivative analysis

The transition slope between points with different quantum efficiency is defined as the values taken by the dI_{SC}/dl derivative, which is related to the laser beam size. As it has been aforementioned, the smaller the spot size, the more abrupt the I_{SC} transition between points with a different superficial photoactivity and the larger the absolute value of dI_{SC}/dl. If the dl is constant, then the derivative can be easily obtained as the dI_{SC}.

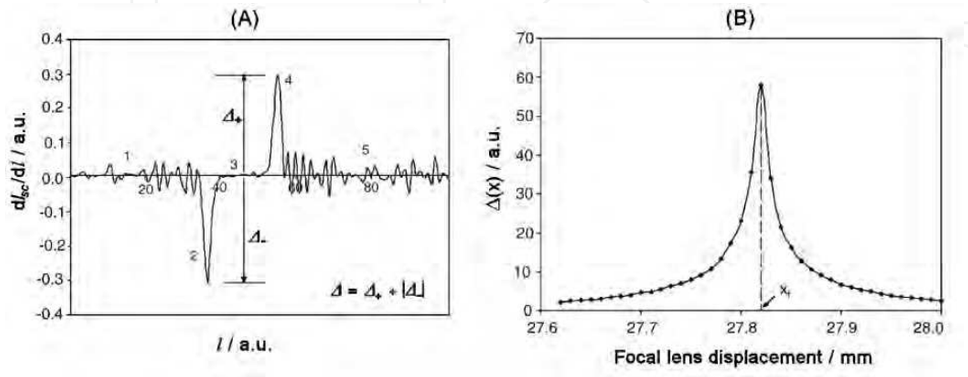

Fig. 3. (A) Numerical derivative of the I_{SC}-curve shown in Figure 2A. (B) Representation of the Δ value versus positions of the focal lens.

Figure 3A shows the derivative of the I_{SC}-curve previously shown in Figure 2A in a way that makes possible to recognize the above-mentioned one to five zones. Attention should be drawn to the fact that the absolute maximum values of the derivative are associated to transitions between photoconversion units with greater differential quantum efficiency. From this representation a new magnitude called Δ can be defined as the absolute difference between the maximum and minimum:

$$\Delta=\Delta_{+}-\Delta_{-}=\max\left(\frac{dI_{SC}(l)}{dl}\right)-\min\left(\frac{dI_{SC}(l)}{dl}\right). \quad (5)$$

At this point it is very easy to conclude that, the smaller the spot size (focused laser beam), the higher Δ value. Then, the representation of Δ according to the focal lens position, x, must result in a Focal-curve showing a peak distribution (Figure 3B). In it, the optimum focusing position, x_f, corresponds to that one in which the value of Δ is the maximum.

3.3 Treatment of the Focal-curve

The determination of the x_f position from the Focal-curve can be accomplished by numerical or algebraic methods. In both cases, several artifacts that habitually appear in the Focal-curve obtained as noise, asymmetric contour or multipeaks must be minimized. To diminish the associated noise to each scan point of the Focal-curve, the applying of an accumulation method is the more appropriated way, either to individual points or to full scans. However, the other two artifacts do not show a clear dependence on known procedures. Normally, discerned or undiscerned multilevel photoactive structures can lead to obtain multipeaks and asymmetric contours, but other several circumstances can be cause of them. No particular dependence of these artifacts with the experimental methodology (EM1 or EM2) or with the derivative analysis system has been observed. To apply the numerical method, it

is enough to determine the focal lens position in which the peak distribution shows a maximum, and to associate that value with x_f. This is a very quickly methodology but shows significant errors and limitations due to the aforementioned artifacts. The maximum obtainable resolution with this method depends on the incremental value used in the focal lens positioning. A resolution improvement in one order of magnitude implies to measure a number of data two greater orders of magnitude. In the other side, the algebraic method involves adjusting a mathematical peak function to the Focal-curve and then determining x_f as the x value that maximizing the adjusted mathematical peak function. This methodology makes it possible mathematically to determine the maximum of the adjusted curve with as much precision as it is necessary.

In previous tests carried out by means of computerized simulation techniques it was demonstrated that a Pseudo-Voigt type 2 function is one of the peak functions that allows a better adjustment (Poce-Fatou et al., 2002; Fernández-Lorenzo et al., 2006). This function is a linear combination of the Gauss and the Lorentz distribution functions, i.e.

$$V(x)=V_0+V_m\left[sf\frac{2}{\pi}\frac{w_L}{4(x-x_f)^2+w_L^2}+(1-sf)\frac{\sqrt{4\ln 2}}{\sqrt{\pi}w_G}e^{-(4\ln 2/w_G^2)(x-x_f)^2}\right], \quad (6)$$

where V(x) represents the values of Δ, L or ϕ according to the position of the focal lens, w_L and w_G are the respectively FWHM (Full Width at Half Maximum) values of the Lorentzian and Gaussian functions, V_m is the peak amplitude or height, sf is a proportionality factor, V_0 is the displacement constant of the dependent variable and x_f is the curve maximum position.

With this focusing system and algorithm, a spot size of 7.1 x 10^{-12} m^2 is easily obtained.

4. LBIC under trichromatic laser radiation: approximation to the solar radiation

Using lasers as the irradiation source is the best solution in LBIC technique as they have a highly monochromatic emission with a quasi parallel beam with minimal divergence and Gaussian power distribution in TEM_{00} mode. These characteristics allow them to be focalized with maximum efficiency. However, using monochromatic radiation beams means that the maps obtained are only representative of the photoefficiency at the wavelength of this type of radiation, and it is not possible to obtain measurements of how the behavior of the system is different at other wavelengths. So, studying the same area with a red-green-blue trichromatic model makes it possible to create characteristic maps associated with each wavelength. Combining them in a suitable way, with irradiation power ratios regulated following a standard emission such as Planck's law or solar emission, makes it possible to approximate to the behavior of the photovoltaic device when it is irradiated with polychromatic radiation, for example, solar emissions. In the literature, it is possible to find a work where LBIC images under solar radiation are obtained (Vorster and van Dyk, 2007). This system uses, as irradiation source, a divergent lamp by which the spot diameter obtained in the focus is about 140 μm and a low spatial resolution can be obtained. So, the methodology that we describe here is a first approach for obtaining high resolution LBIC images that approximate the behavior of a photoactive surface under solar radiation.

The first approach is to assume that the solar emission was blackbodylike with a temperature of 5780 K, as we can assume from literature data (Lipinski et al, 2006). The energy distribution emitted by a black body can be expressed using the Planck's equation

$$Me(\lambda)=\frac{8\pi hc}{\lambda^5}\frac{1}{\exp(hc/\lambda kT)-1}, \quad (7)$$

where h is the Planck constant, c the speed of light, k the Boltzmann constant, T the absolute temperature, and λ the wavelength.

With the lasers used in our system, which are described above, in section 2, using Planck's law and setting the initial irradiation power value, the power of the red laser (632.8 nm), as P_0, the irradiation power for the other two lasers is calculated to be $1.12P_0$ for both casually. By means of this ratio, the relative powers of the three wavelengths are close to the profile of solar radiation. These three wavelengths are placed in the range of the maximum irradiance in the solar spectrum or black body emission curve, i.e., around the maximum of the energy emission.

4.1 Working procedure

The main features for obtaining representative quantum efficiency maps of a photoactive surface are related with the geometry of the system and the different positioning parameters of the optical elements of the system. Furthermore, with the trichromatic system shown in this chapter, it is necessary to take into account the relative irradiation power of the lasers and the unification of the three optical pathways. Thus, the most relevant aspects in the system are considered in the following way:

1. The angle of incidence of the laser must be normal to the photoactive surface in order to minimize the size of the spot. The incidence of the laser beam used perpendicular to the surface can be assured by observing the reflected radiation, the trajectory of which will only coincide with the incident radiation if it is perpendicular to the photoactive surface. Furthermore, this is a necessary condition when trying to obtain reflectance maps correlatable with photoefficiency maps, in accordance with the optical geometry used.
2. The distance between the focal lens and the point of incidence on the surface must remain constant, independent of the laser incidence coordinates over the surface which is derived from the y-z movement of the motorized platform. Thanks to the system being completely automated and controlled by specially designed software, the focusing positions are stored and saved for later use.
3. With the beam selector mirror, the optical trajectory of each of the lasers used must coincide completely with the others, and furthermore, all of them must come into contact on the photoactive surface with the right power to generate radiation resembling that of the black hole, as mentioned earlier.

The bidimensional scans of the surface under study are performed in sequence; first, opening the shutter of the active laser and positioning the mirror; then, setting the focusing lens at the right distance according to the laser to be used; and finally, establishing the irradiation power for each of the lasers. Under these conditions, using the photocurrent values generated in each scan, it is possible to obtain the quantum efficiency values for the device. Thus, using the spectral response, it is possible to obtain a matrix of the external quantum efficiency of the scans performed, following the expression

$$[EQE(\lambda)]_{ij}=[SR(\lambda)]_{ij}\frac{hc}{e\lambda}, \quad (8)$$

where EQE(λ) is the external quantum efficiency, SR(λ) the spectral response, e the elementary charge, h the Planck constant, c the rate of the light, and λ the wavelength.

Taking the definition of the spectral response to be the relationship between the photocurrent generated and the irradiation power, the external quantum efficiency is

$$[EQE(\lambda)]_{ij}=\frac{[I_{SC}(\lambda)]_{ij}}{P_{in}(\lambda)}\frac{hc}{e\lambda}, \quad (9)$$

where $I_{SC}(\lambda)$ is the short-circuit current generated and $P_{in}(\lambda)$ the irradiation power. Likewise, it is also possible to obtain internal quantum efficiency matrixes following

$$[IQE(\lambda)]_{ij}=\frac{[EQE(\lambda)]_{ij}}{1-[R(\lambda)]_{ij}}=\frac{[I_{SC}(\lambda)]_{ij}}{P_{in}(\lambda)}\frac{hc}{e\lambda}\frac{1}{1-[R(\lambda)]_{ij}}, \quad (10)$$

where IQE(λ) is the internal quantum efficiency and R(λ) is the reflectance.
After calculating the three matrixes of quantum efficiency (internal or external), a colour image can be created reflecting the behaviour of the device under irradiation with the three wavelengths used. To do this, an image analysis program is used which adapts each value of the matrixes obtained to a common scale between 0 and 255 for the three colours red, green and blue; then the three matrixes are combined to obtain a colour image. This image provides information about the behaviour of the material under irradiation with the three wavelengths used.
Furthermore, using the data matrixes obtained, micrometric quantum efficiency values can be obtained which are approximate to those which would be obtained under solar irradiation, as the irradiation power values were set applying Planck's law. Mathematically, according to this approximation, the external quantum efficiency can be expressed as

$$\left[(EQE)_{ij}\right]_{solar}=\frac{hc}{e}\left[\frac{\left[(I_{SC})_{ij}\right]_{632.8nm}+\left[(I_{SC})_{ij}\right]_{532nm}+\left[(I_{SC})_{ij}\right]_{473nm}}{[P_{in}\lambda]_{632.8nm}+[P_{in}\lambda]_{532nm}+[P_{in}\lambda]_{473nm}}\right], \quad (11)$$

where all the variables have been defined above, and they are expressed for the wavelengths of the laser beam used in each of the scans.
So, the method described in this work investigates the photoresponse of the devices to study at three specific wavelengths. The relative flux distribution of the three wavelengths attempt to match the corresponding wavelengths in the solar spectrum. Obviously, this methodology is an approximation because we attempt to simulate a multispectral radiation as the solar emission with only three specific wavelengths. So, the results obtained will be an approximation to the optoelectrical behavior of the devices under solar illumination.

5. Algorithm for improving photoresponse of dye-sensitized solar cells

Dye-sensitized solar cell (DSSC) is an interesting alternative to photovoltaic solar cells based on solid-state semiconductor junctions due to the remarkable low cost of its basic materials and simplicity of fabrication. DSSC technology enables the flexible combination of different substrates (PET, glass), semiconducting oxides, redox shuttles, solvents and dyes (O'Regan and Grätzel, 1991). When a DSSC is illuminated in the range in which the dye absorbs light, the dye molecules are excited to upper electronic states, from which they inject electrons into the conduction band of the semiconductor. The dye molecules become oxidized, whereas the photogenerated electrons diffuse through the semiconductor nanostructure until they are collected by the front electrode. The electrolyte with the redox pair plays the role of a hole conductor, regenerating the oxidized dye molecules and transporting electron acceptors towards the counter electrode. A scheme of a typical DSSC is shown in Figure 4.

Due to the existence of two distinct phases, an electron conducting region and a liquid electrolyte, the electrical response of the device under illumination is not immediate. In contrast, it takes some time (in the order of seconds) before it reaches and keeps its maximum value. This is the socalled characteristic response time. Furthermore, once the irradiation is interrupted, the electrical signal does not disappear instantaneously, but it decays smoothly. This decay time is related to the electron lifetime in the semiconductor (Fredin et al., 2007) and depends on both the trap-limited diffusion transport in the semiconductor (Peter, 2007) and the specific kinetics of the electron transfer reaction in the liquid phase (Gregg, 2004). The decay features in this case can be viewed as a charge/discharge process typical of a capacitor. Rise and decay times should be taken into account when employing techniques to measure quantum yields in DSSCs.

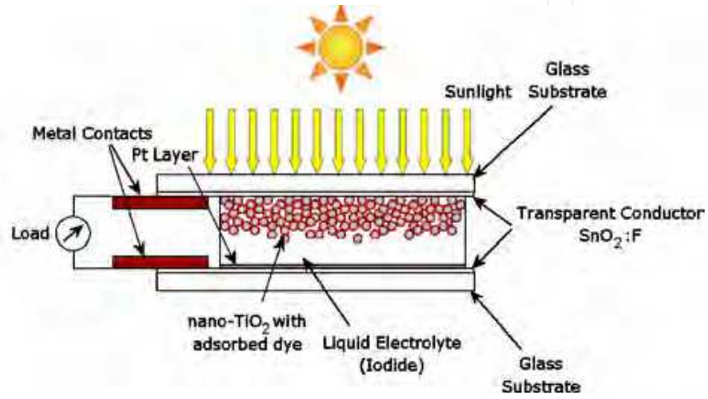

Fig. 4. A scheme of the structure and components of the dye-sensitized solar cells.

The LBIC technique has not been used commonly to characterize DSSCs due to the blurring effect of the slow response of the device to optical excitation and subsequent decay. Hence, to get good spatial resolution the laser beam has to be focused on a very narrow spot. This produces local heating and degradation of the dye/oxide system. This problem can be surmounted by using filters that reduce the light intensity. However, this strategy also reduces the photoconversion signal, which must be amplified to get significant results. Furthermore, as mentioned above, excitation of a single spot requires stopping the scan so that the signal is stabilized properly. This increases the chances of degradation and the time length of the experiment. Hence, a time of 5 s for the rise and decay processes (typical in many DSSCs) implies that to obtain the LBIC signal, we need to (a) irradiate the spot, (b) wait 5 s until the maximum value of the signal (either photocurrent or photovoltage) is achieved, (c) stop the illumination and wait another 5 s until the signal reaches its minimum value and (d) move forward to the next spot and repeat the process. For example, using this procedure we would need 29 days to scan a 500 × 500 μm^2 cell with 1 µm resolution. In summary, in contrast to silicon solar cells, to obtain clear LBIC images for DSSCs is a difficult task if the standard procedure is used.

Many papers can be found in the literature regarding the response time in DSSCs as a function of the composition and structure of the semiconductor (Cao et al., 1996) and the kinetics of the recombination reaction from open circuit voltage decays (Walker et al., 2006). In this chapter we show an experimental view of the rise and decay signal in DSSCs and the empirical equations that describe their time dependence. Starting from the kinetic constants derived from the experiments, we have devised a mathematical algorithm that makes it possible to correct the photocurrent data so that reliable quantum yields can be extracted.

So, in this chapter, we show a methodology for evaluating and correcting the effects of the charge/discharge processes of DSSCs, enabling clear, high-resolution LBIC images to be obtained without having to increase the scanning time. The methodology is based on a simple, prior evaluation of the time evolution of the photosignal for the charge/discharge processes, before establishing a mathematical algorithm applied point by point over the signal of the cell registered during the LBIC scan, correcting the contribution of previously illuminated points to subsequent ones.

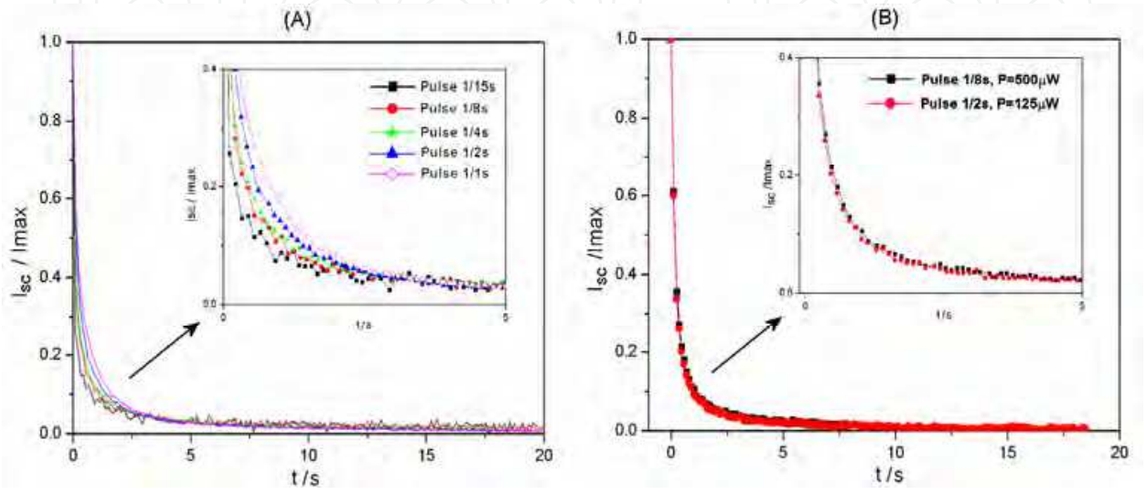

Fig. 5. (A) Time-evolution curve of the discharge process for a cell irradiated with a 532 nm laser, a power of 350 μW, and different exposure times to the radiation. (B) Comparison of two time evolution curve of the discharge process in which the photonic energy is identical but has been generated with different irradiation power and exposure time.

5.1 Methodology description

The methodology developed is based on the evaluation of time-evolution curves of the response times for charge/ discharge processes. Based on this, an algorithm corrects the contributions of previous points to the signal of the active one. To perform an LBIC scan within a reasonable time requires dwell times in the order of milliseconds at each point of the scan. This means the system acts as if it were subjected to a set of light pulses, one for each point of the scan. The response of the system depends on the amount of energy received in each pulse. Figure 5A shows time-evolution curves of the photosignal generated by a DSSC at different pulse times using a 532 nm laser and irradiation power of 350 μW. The decay curve is not the same in all cases but rather it depends on the exposure time of the irradiated point. Figure 5B shows two time-evolution curves for the photosignal, one with a 1/8 s pulse and an irradiation power of 500 μW and the other a 1/2 s pulse with an irradiation power of 125 μW so the amount of energy in both cases is constant. This graph shows that the cell behaves the same in both cases, implying that the response during the discharge process of each irradiated point depends on the light energy received. That is, the product of the irradiation power and exposure time. Thus, it is necessary to set the irradiation conditions to be used for performing the scan with the LBIC system in order to obtain the charge/discharge curves of the cell under study under the same conditions.

5.1.1 Setting irradiation conditions

Setting the conditions for performing the scan depends on the cell under study, particularly those conditions related to the dwell time of the laser on each point and the amount of energy received. Among these factors are these following considerations: (a) dimensions of the surface to scan, (b) spatial resolution or the distance between points, (c) irradiation power, and (d) dwell time for each point. For the dwell time, the total exposure time must be considered, even when measurements for each point are taken more than once to average the results. From these data the total number of photons affecting each irradiation point can be established with their overall total composing the LBIC image.

5.1.2 Determining the time-evolution curves

With the irradiation conditions set, the time-evolution curves for the charge/discharge processes of the cell under study are then developed. To do this, one point of the cell is irradiated with the same amount of photonic energy to be used during the scan. Using a continuous emission laser, irradiation conditions can be established by using a set of neutral density filters and a shutter, such as, for example, the body of a reflex photographic camera. During the selected pulse time, until the system stabilizes, the evolution of the photosignal is recorded. The data obtained for the discharge process are adjusted to a decreasing exponential function following the equation

$$I_{SC}=I_r+I_0 \cdot e^{-A_{SC}t}\,, \tag{12}$$

where I_{SC} is the short circuit photocurrent, I_r is the residual current remaining in the system, I_0 is the short circuit steady-state photocurrent, A_{SC} is the rate constant of the discharge process, and t is the time. Using this equation and with specifically designed software, simulations of the photogenerated signal have been developed, which prove the initial hypotheses for the application of this methodology. It is seen that the smaller the rate constant the greater the influence of the discharge process in the LBIC image. Also, it is also concluded that the limit intensity (I_{lim}) that the signal of a cell can reach depends on the relationship between the velocity constants of the charge (A_{SCC})/discharge (A_{SCD}) process and the short circuit steady-state photocurrent, expressed as

$$I_{lim}=I_0 \frac{A_{SCC}}{A_{SCD}}\,. \tag{13}$$

Furthermore, in most cases, but not always, it is observed experimentally that charge process is faster than the discharge process so the charge process has less influence. In Figure 6A, the charge process lasts about 7 s, while the discharge process takes approximately 16 s. Correcting the charge process effect in the algorithm involves a simple change of scale depending on the response time, calculated with the data of the time-evolution curves and the dwell time. Thus, the correction derived from the charge process, involving multiplying the signal by the correction factor, does not result in a substantial improvement in the quality of the LBIC images. However, it is fundamental for calculating the cell's quantum efficiency. Consequently, the algorithm is based on correcting the contributions of the previously irradiated points, which depend on the discharge process, and correcting the signal level due to the charge process. The time-evolution curves are obtained with the laser beam focalized on one point of the photoactive surface, accepting

that no dependency exists with regards to the position of this point since the discharge process can be associated with the diffusion processes occurring inside the cell.

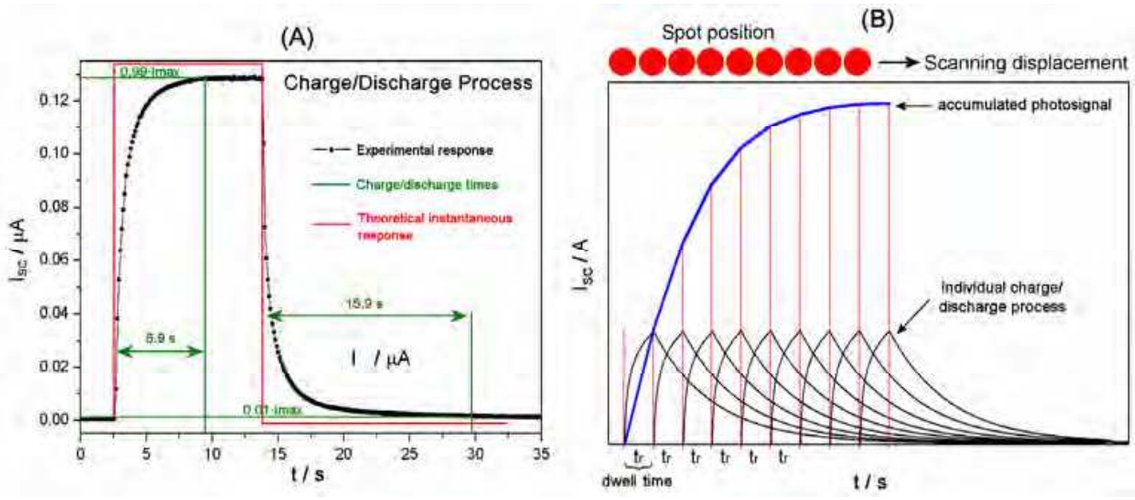

Fig. 6. (A)Representation of experimental data of the charge and discharge process of a cell irradiated with a power of 292 μW, and a comparison with a theoretical instantaneous response. (B) Simulation of the evolution of the irradiated sports showing how the photovoltaic response is influenced by the previously excited points.

5.1.3 Correcting the LBIC image

Now, the correction of the discharge process will be describe. From the equation obtained for the cell, the experimental values obtained while taking the LBIC image are corrected, thus eliminating the contribution of the previously irradiated points to the photosignal. The number of points of the scan to be considered as contributing to the signal of one given point is a characteristic of the cell under study and depends on the characteristic parameters of the discharge curve, as is shown in Figure 6B. To evaluate the number of points, the experimental values of the time evolution of the discharge process are adjusted to equation (12), and the time necessary for total discharge is taken as being from when the signal is below 1% of the maximum registered value of the photosignal for that cell in those measuring conditions. With this time, and the dwell time, it is possible to obtain the number of points that have to be considered as contributing to the signal measured and whose contribution has to be corrected to apply the correction to the original image. The extent of this contribution is established using equation (12) and the adjustment parameters obtained, depending on the time passed since a point has been irradiated.

Thus, the real photocurrent signal generated by the irradiated point of the cell is defined as the difference between the photocurrent measured (I_m) and the contribution of the previously irradiated points. This is expressed mathematically using the equation

$$I_{SC}=I_m-\sum_{i=1}^{i=n}\left(I_r+I_0\cdot e^{-A_{SC}it_r}\right)=I_m-nI_r-I_0\sum_{i=1}^{i=n}e^{-A_{SC}it_r}\,, \tag{14}$$

where I_{SC} is the real short circuit photocurrent generated at the active point, I_m is the signal measured at that active point during the LBIC scan, n is the number of previously irradiated points to consider, t_r is the dwell time; the other variables have been defined above.

6. Applications

In order to test the system described here, LBIC scans were performed on various samples. We show results obtained using three different kind of solar cells such as a polycrystalline silicon solar cell, an amorphous thin film silicon solar cell, and a dye-sensitized solar cell.

6.1 Polycrystalline silicon solar cell

We include the results obtained with a polycrystalline silicon solar cell manufactured by ISOFOTON, S.A. Different studies were carried out on this device with differing degrees of resolution. Groups of the scans performed with the three lasers are shown below.

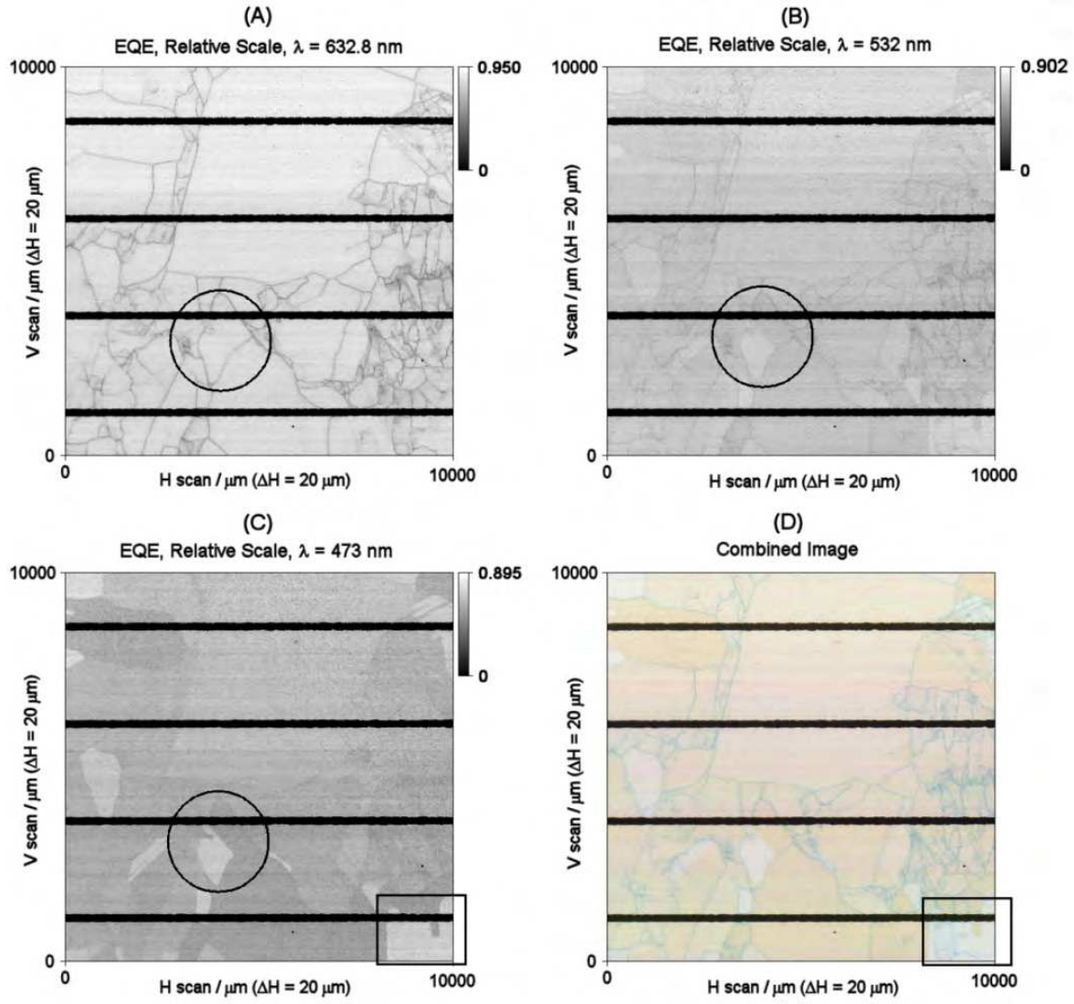

Fig. 7. LBIC images of the three scans performed and the image created by combining these. The data used to construct these images are of EQE on a relative scale for each image.

First, LBIC scans were carried out with the three lasers mentioned above on a 1x1 cm^2 area of the surface of the cell with a resolution of 20 μm. The irradiation power for the red laser was 5 μW, and 5.6 μW for the green and blue ones. These values comply with the emission of a blackbody at 5780 K, in accordance with Planck's law (equation (7)). Figure 7 shows the

images obtained for the three scans, each one using EQE data on a relative scale. That is, a scale of greys is used which are between the maximum and minimum EQE for each of the images (A-B-C). From Figure 7 it is possible to observe that the conversion of the device depends on the irradiation wavelength used. Macroscopically, a greater quantum efficiency, or photoconversion, is observed when the cell is irradiated with the red laser. This can be seen clearly in Figure 7D, a combined image using those obtained in the scans with each of the lasers, and in which the colour red is seen to dominate most of the image. There are regions where red is not the predominant colour (e.g. the area shown with a square), due to the conversion being greater for one of the other lasers. However, the conversion with blue radiation is similar to that obtained with red. Microscopically, differences can be seen in the scans performed depending on the wavelength used, such as in the area marked with a circle in the images in Figure 7. Furthermore, the maximum and minimum EQE values in each scan are shown in table 2. From these values, an increase in conversion of between 5 and 6 % can be seen in the scan performed with the red laser (632.8 nm) compared with those carried out with the green (532 nm) and blue (473 nm) lasers, just as we had concluded qualitatively before from a simple visual observation.

λ / nm	EQE		λ / nm	EQE	
	Maximum	Minimum		Maximum	Minimum
632. 8	0.950	0	473	0.895	0
532	0.902	0	Approximation to sunlight	0.917	0

Table 1. Maximum and minimum EQE values for the scans performed and the image obtained as an approximation to solar irradiation.

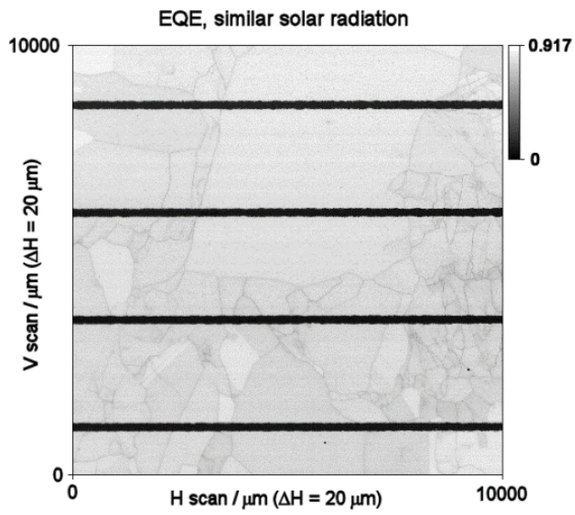

Fig. 8. EQE image approximated to solar radiation using equation (12).

Also, from equation (11) it is possible to obtain EQE values which should be an approximation of the result which would be reached if the device were subjected to solar radiation (see figure 8). The maximum and minimum values obtained are shown in table 1. It is observed that the maximum EQE value for the image constructed with the approximation to solar irradiation is among the maximum values for the three scans

performed. In turn, using the EQE values, an image was constructed using the procedure described which approximates the behaviour of the cell under solar radiation.

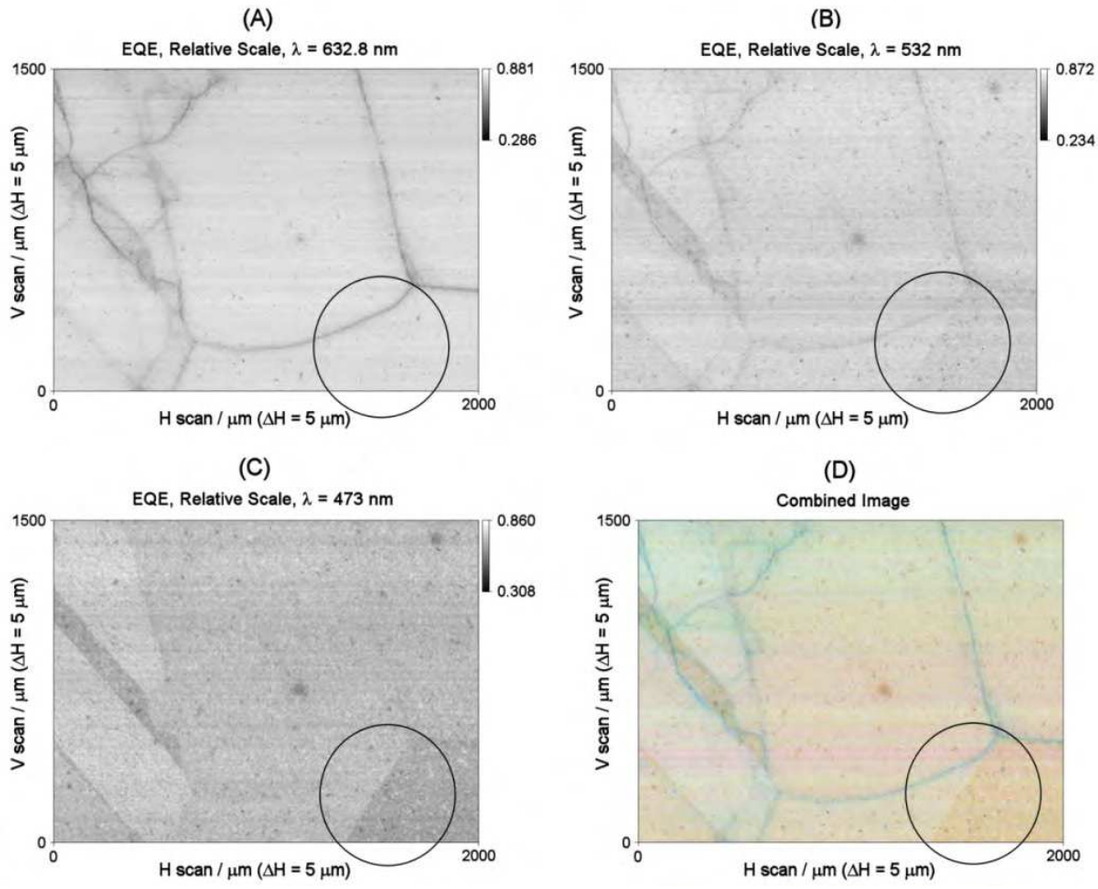

Fig. 9. LBIC images of the three intermediate resolution scans performed using EQE values on a relative scale for each image and the combined image using all three.

Secondly, scans are shown which were performed on a small surface area, but with greater resolution. The surface area scanned was 2x1.5 mm^2 with a resolution of 5 μm. The irradiation conditions were the same as those described above. Figure 9 shows the three scans performed, as well as the combined image. In this figure it is possible to observe small differences in the photoelectric properties of the device depending on the laser used. In the area marked with a circle two clearly distinct regions of differing quantum efficiency can be observed with the green and blue lasers, something which does not happen with the red laser. This difference in efficiency between the two zones becomes more pronounced as the wavelength is reduced. In other words, the depth of penetration decreases, and so we can conclude that this difference in efficiency is due to an artefact on the surface of the cell. It is also possible to observe that the definition of the grain boundaries depends on the wavelength used to do the scan, with the longer wavelength (red laser) leading to better definition, while with the blue laser (shorter wavelength) the grain boundaries can hardly be seen. We will study in greater detail below the differences which can be observed in the grain boundaries depending on the wavelength of the laser.

The maximum and minimum EQE values in each scan are shown in table 2. From these values, greater conversion can be observed in the scan performed with the red laser compared with those performed with the green and blue ones.

λ / nm	EQE		λ / nm	EQE	
	Maximum	Minimum		Maximum	Minimum
632. 8	0.881	0.286	473	0.860	0.308
532	0.872	0.234	Approximation to sunlight	0.873	0.284

Table 2. Maximum and minimum EQE values for the 2x1.5 mm^2 scans and those which would be obtained as an approximation to solar irradiation.

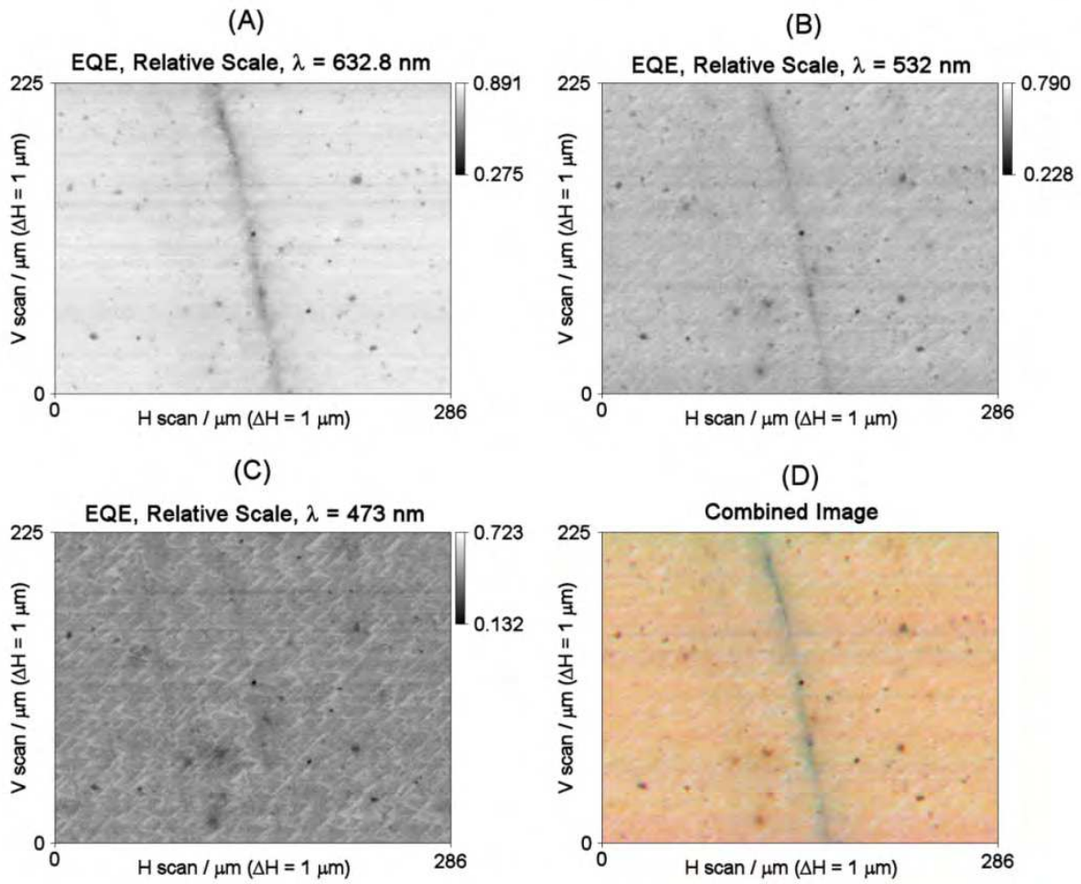

Fig. 10. LBIC images obtained of the three high resolution scans (1 μm) performed using EQE values on a relative scale for each image and the combined images using all three.

Thirdly, high resolution scans were performed. The scans covered a surface area of 286x225 μm^2, and were performed with a spatial resolution of 1 μm. The irradiation conditions were those described above for the two previous examples. Figure 10 shows the images obtained from the three scans performed. In the images obtained with the red laser, a perfectly defined grain boundary can be observed. On the other hand, this grain boundary is practically impossible to see in the scan performed with the blue laser due to the

difference in the absorption coefficient, which depends on the irradiation wavelength and thus in the difference in the depth of penetration. The green laser provides results halfway between the others. If we wanted to obtain information about carrier diffusion lengths from the grain boundary, the results would differ depending on the irradiation wavelength used. Figure 11 shows the profiles that would be obtained for each scan. These profiles have been obtained as an average of all the horizontal profiles of the scans performed and setting the minimum photocurrent value on the grain boundary common to all the profiles of each scan. Thus, it can be observed that the LBIC signal is influenced in a larger region from the grain boundary as the wavelength increases. These profiles could make it possible to obtain diffusion length values, for example by following the model presented by Yagi et al. using the analysis of the electrical properties of grain boundaries in polycrystalline silicon solar cells (Yagi et al. 2004). But as Figure 11 shows, it would be necessary to bear in mind the irradiation source used.

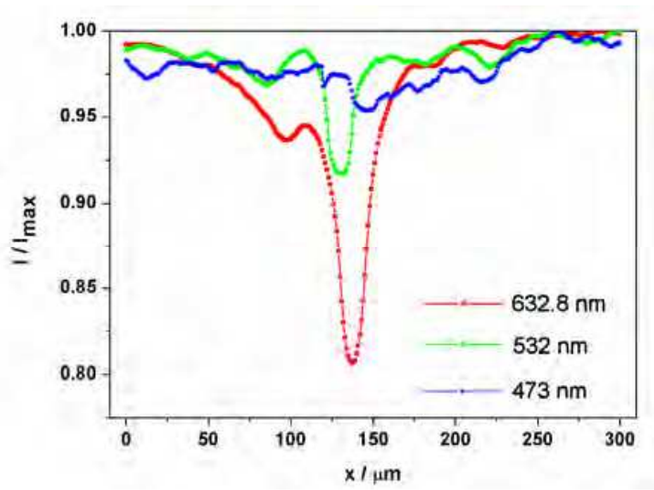

Fig. 11. Average LBIC signal profiles obtained for each of the three high resolution scans performed of a grain boundary.

6.2 Amorphous thin film silicon solar cell

We include the results obtained with an amorphous thin film silicon solar cell manufactured by GADIR SOLAR, S.A. LBIC scans were carried out with the three lasers on a 350x350 μm^2 area of the surface of the cell and were performed with a spatial resolution of 1 μm. The irradiation power for the red laser was 335 μW and 375 μW for the green and blues ones. These values comply with the emission of a blackbody at 5780 K, in accordance with Planck's law. Figure 12 shows the images obtained for the three scans, each one using EQE data on relative scale (maximum and minimum EQE for each of the images A-B-C). The scanned surface is the zone where the solar cell has been marked by laser ablation in order to separate the different cells that make up the solar cell. In the Figure 12 we can see that the laser marking is composed of three lines made point by point with different diameter which leads to the width and depth of each line is different. In the images obtained using the red laser, the three lines are perfectly defined, but it is difficult to see in the scans performed with other two lasers. In turn, macroscopically, greater quantum efficiency is observed

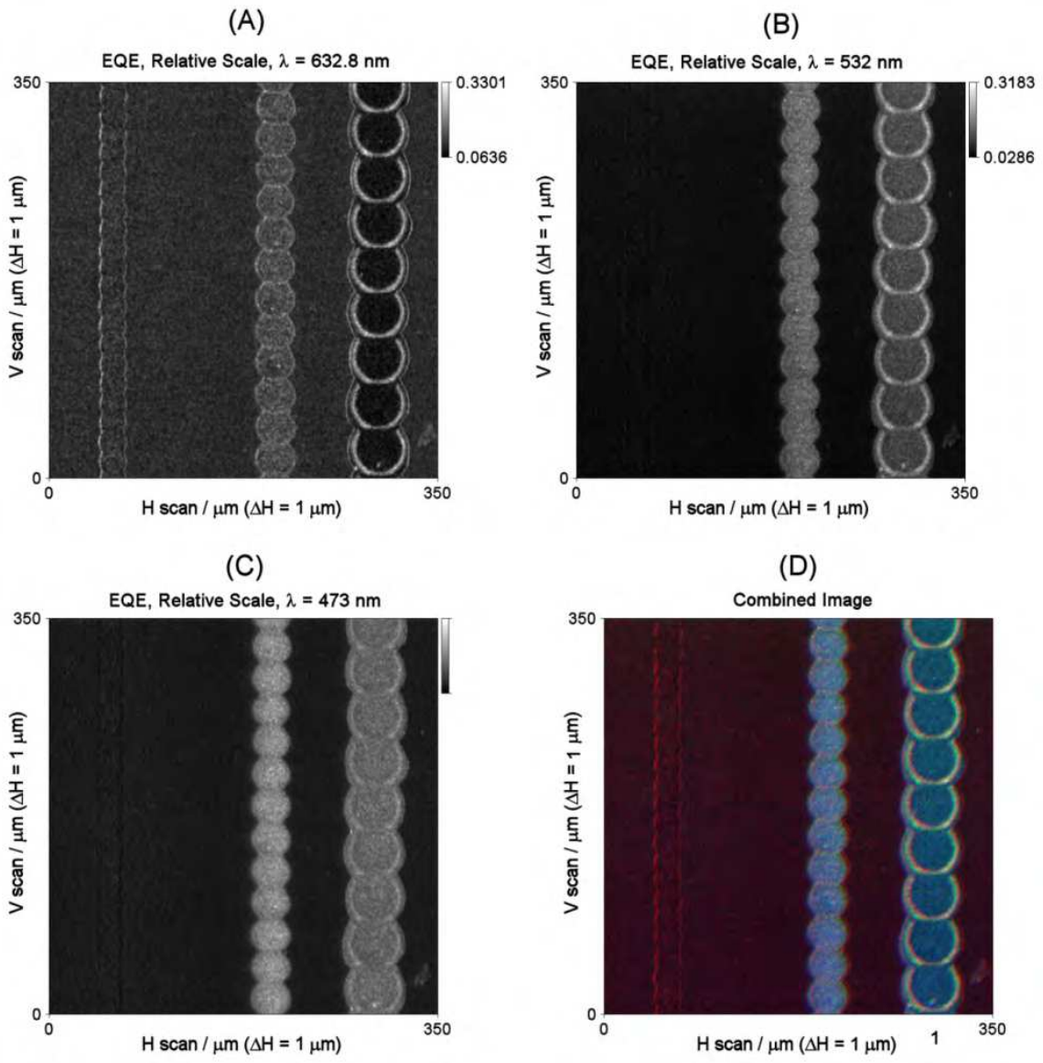

Fig. 12. LBIC images of the three high resolution scans performed using EQE values on a relative scale for each image and the combined image using all three.

when the cell is irradiated with the red laser. This can be seen clearly in Figure 12D, a combined image using those obtained in the scans with each of the lasers, and in which the color red is seen to dominate most of the image. In the zone inside of two of the lines, the red color is not predominant, due to the conversion being greater for one of the other lasers.

λ / nm	EQE		λ / nm	EQE	
	Maximum	Minimum		Maximum	Minimum
632. 8	0.330	0.064	473	0.303	0.011
532	0.318	0.029	Approximation to sunlight	0.237	0.048

Table 3. Maximum and minimum EQE values for scans of an amorphous thin film silicon solar cell and those which would be obtained as an approximation to solar irradiation.

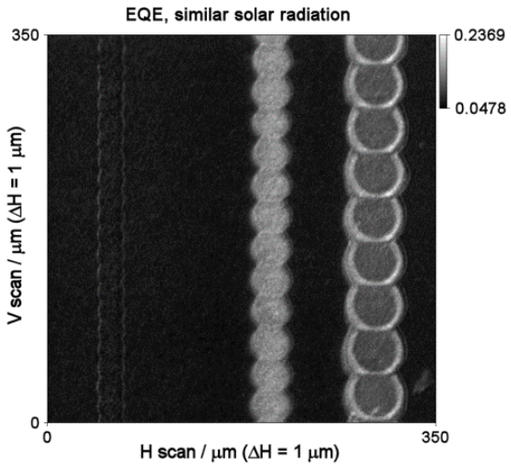

Fig. 13. EQE image approximated to solar radiation using equation (14) for an amorphous thin film silicon solar cell.

The maximum and minimum EQE values in each scan are shown in table 3. From these values, a decrease in conversion of 4 and 8 % can be seen in the scans performed with green laser and blue one, respectively. From equation (11) it is possible to obtain EQE values which should be an approximation of the result which would be reached if the device were subject to solar radiation. The maximum and minimum EQE values in this case are shown in table 4. In turn, an image using EQE values approximated to solar radiation has been constructed using the procedure describes previously. This image is shown in Figure 13.

6.3 Dye-sensitized solar cell

The dye-sensitized solar cell used in this chapter was made by authors following the next procedure: Two fluorine-doped tin dioxide coated transparent glass plates (2x2 cm^2 sheet resistance ~ 15 Ω $square^{-1}$) supplied by Solaronix were used as the electrode and counter-electrode. Using nanoparticulated TiO_2 with a nominal particle size of 25 nm, supplied by Degussa Co., a paste was developed using nitric acid and ethanol at a proportion of 1:3.25. A thin layer of paste was deposited on the electrode plate using the doctor blade method and sintered at 450 °C for 1 h. The thickness of the TiO_2 films was 9±0.5 μm. A mixture of 0.5*M* 4-tert-butylpyridine, 0.1*M* lithium iodide, and 0.05*M* iodine in 3-methoxypropionitrile as a solvent, was used as an electrolyte. A catalytic layer of Pt was deposited on the counter-electrode by decomposing a superficially sprayed solution of 0.01*M* H_2PtCl_6 in 2-propanol at 380 °C. Finally, the electrode plate with the sintered layer of TiO_2 was immersed in dye solution. The dye used was an ethanolic solution of Ru535 (formerly known as N3, $C_{26}H_{20}O_{10}N_6S_2Ru$).

LBIC scans were carried out with the three lasers mentioned above on a 300x300 μm^2 area of the surface of the cell and were performed with a spatial resolution of 1 μm. In accordance with Planck's law, the irradiation power for the red laser was 6.62 μW, and 7.41 μW for the green and blues ones. First, the photocurrent values obtained from the three scans were corrected using the algorithm described in section 5. The LBIC images built from photocurrent values measured are shown in Figures 14A, 15A and 16B for lasers red, green and blue, respectively. The images built using the corrected values are shown in Figures

14B, 15B and 16B. In turn, in Figures 14-16 the histograms of the photocurrent values, in both cases, are shown. In these histograms, for the three lasers, it is observed that the measured photocurrent values are higher than the photocurrent values obtained after applying the algorithm. This is obvious because each measured point of the cells has contributions from the previously irradiated (an effect that can be easily observed in Figure 6). The corrected images (Figures 14B, 15B, and 16B) display improvement in clarity. These improvements can be easily observed in the scans made with the red laser, where the artefacts in the surface of the cell can be seen with better definition.
From the values corrected and using the equation (11) the values of EQE can be obtained for each scan. Figure 17 shows the image obtained applying the algorithm described to obtain images which would be obtained as an approximation to solar irradiation. From this image, the maximum and minimum values of EQE are obtained. These values are shown in table 4.

λ / nm	EQE		λ / nm	EQE	
	Maximum	Minimum		Maximum	Minimum
632. 8	0.309	0.096	473	0.265	0.110
532	0.253	0.100	Approximation to sunlight	0.276	0.102

Table 4. Maximum and minimum EQE values for scans of a dye-sensitized solar cell and those which would be obtained as an approximation to solar irradiation.

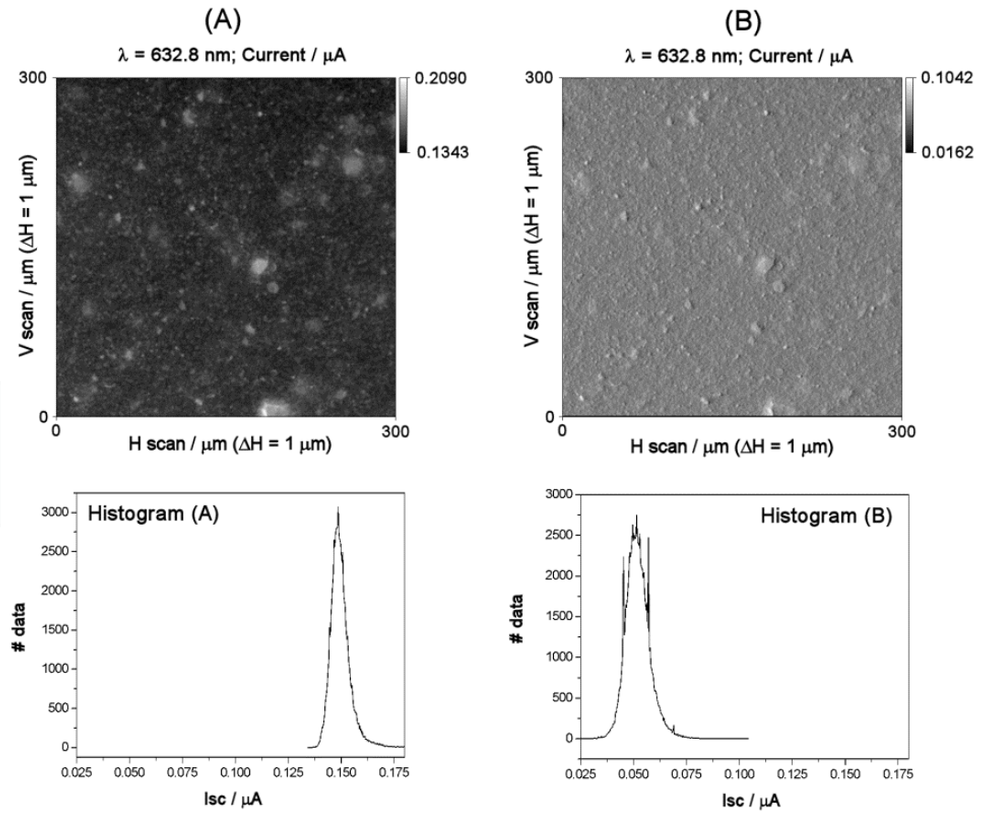

Fig. 14. (A) LBIC image for the DSSC using red laser. (B) The same image modified using our algorithm.

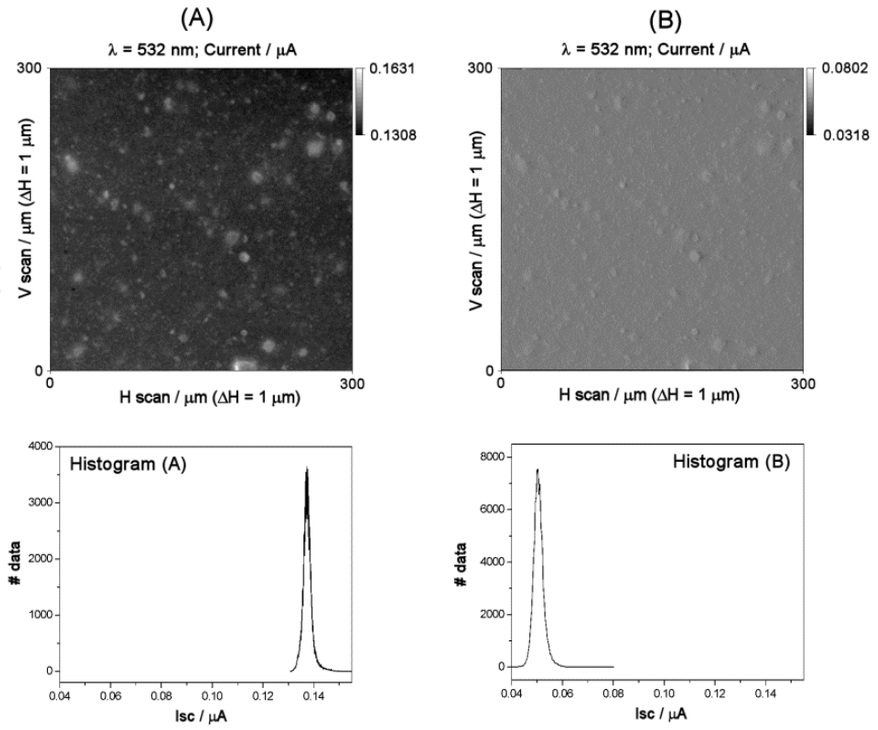

Fig. 15. (A) LBIC image for the DSSC using green laser. (B) The same image modified using our algorithm.

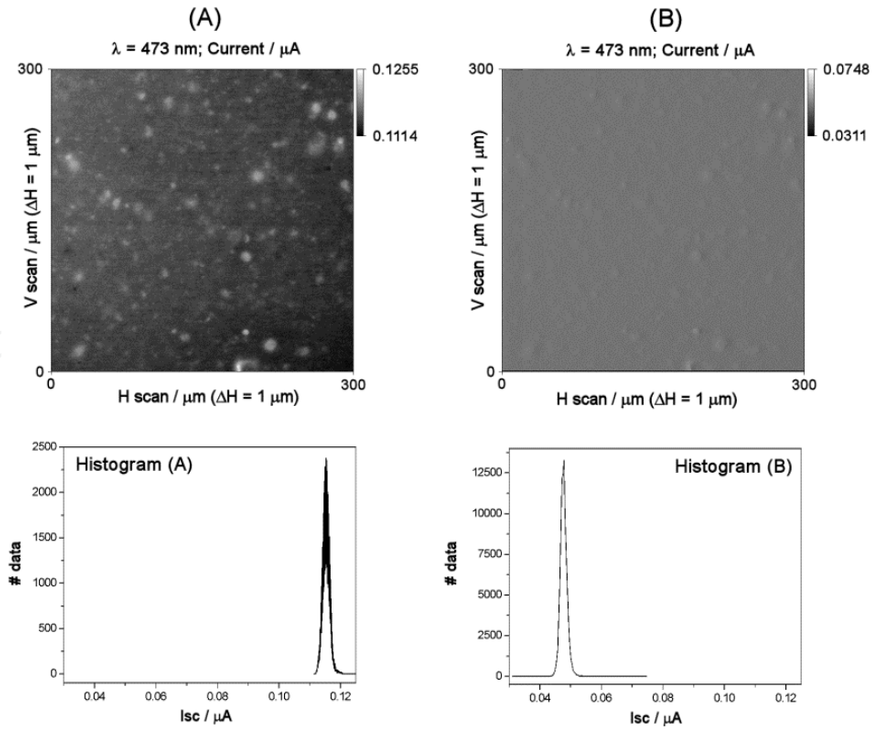

Fig. 16. (A) LBIC image for the DSSC using blue laser. (B) The same image modified using our algorithm.

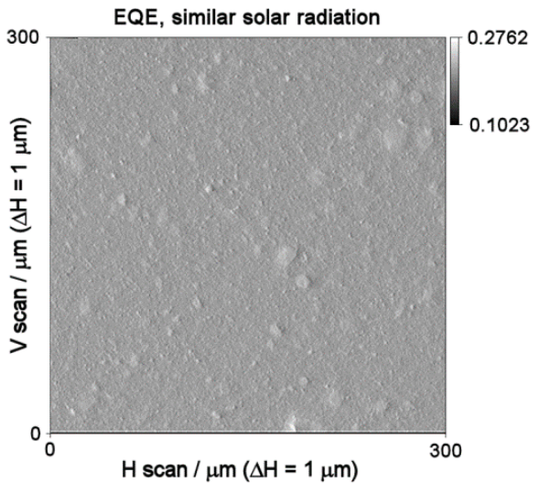

Fig. 17. EQE image approximated to solar radiation for a dye-sensitized solar cell.

7. Conclusions

We have described the fundamentals of computer-controlled equipment for scanning the surface of photovoltaic devices, which is capable of obtaining simultaneously LBIC, and specular reflection/transmittance based images. Several algorithm included in the system have been described. These ones are: (a) the algorithm for focusing the laser beam over the photoactive surface in order to obtain high resolution LBIC images; (b) the algorithm for obtaining images which are approximated to the behavior of photovoltaic devices under solar irradiation conditions, and (c) we have showed the algorithm for improving photoresponse of dye-sensitized solar cells. In turn, we have showed results obtained using three different kinds of solar cells such as a polycrystalline silicon solar cell, an amorphous thin film silicon solar cell, and a dye-sensitized solar cell. In this way, we have tested the goodness of our LBIC system for studying different photovoltaic devices.

8. References

Bisconti, R.; Kous, R.A.; Lundqvist, M. & Ossenbrink, H.A. (1997). ESTI scan facility. *Solar Energy Materials & Solar Cells*, Vol.48, No.1-4, (November 1997), pp. 61-67, ISSN 0927-0248.

Cao, F.; Oskam, G.; Meyer, G.J., Searson, P.C. (1996). Electron transport in porous nanocrystalline TiO_2 photoelectrochemical cells. *Journal of Physical Chemistry B*, Vol. 100, No.42, (October 1996), pp. 17021-17027, ISSN 1520-6106.

Dimassi W.; Bouaïcha, M.; Kharroubi, M.; Lajnef, M.; Ezzaouia, H. & Bessais, B. (2008). Two-dimensional LBIC and internal quantum efficiency investigations of porous silicon-based gettering procedure in multicrystalline silicon. *Solar Energy Materials & Solar Cells*, Vol.92, No.11, (November 2008), pp. 1421-1424, ISSN 0927-0248.

Fernández-Lorenzo, C.; Poce-Fatou, J.A.; Alcántara, R.; Navas, J.; Martín, J. (2006). High resolution laser beam induced current focusing for photoactive surface

characterization. *Applied Surface Science*, Vol.253, No.4 (May 2006), pp. 2179-2188, ISSN 0169-4332.

Fredin, K.; Nissfolk, J.; Boschjloo, G.; Hagfeldt, A. (2007). The influence of cations on charge accumulation in dye-sensitized solar cells. *Journal of Electroanalytical Chemistry*, Vol.609, No.2, (November 2007), pp. 55-60, ISSN 1572-6657.

Gregg, B.A. (2004). Interfacial processes in dye-sensitized solar cell. *Coordination Chemistry Reviews*, Vol.248, No.13-14, (July 2004), pp. 1215-1224, ISSN 0010-8545.

Lipinski, W.; Thommen, D.; Steinfeld, A. (2006). Unsteady radiative heat transfer within a suspension of ZnO particles undergoing thermal dissociation. *Chemical Engineering Science*, Vol.61, No.21, (November 2006), pp. 7039-7035, ISSN 0009-2509.

Navas, F.J.; Alcántara, R.; Fernández-Lorenzo, C. & Martín, J. (2009). A methodology for improving laser beam induced current images of dye sensitized solar cells. *Review of Scientific Instruments*, Vol.80, No.1(June 2009), pp. 063102-1-063102-7, ISSN 0034-6748.

Nichiporuk, O.; Kaminski, A.; Lemiti, M.; Fave, A.; Litvinenko, S. & Skryshevsky, V. (2006). Passivation of the surface of rear contact solar cells by porous silicon. *Thin Solid Films*, Vol.511–512, (July 2006), pp. 248-251, ISSN 0040-6090

Nishioka, k.; Yagi, T.; Uraoka, Y. & Fuyuki, T. (2007). Effect of hydrogen plasma treatment on grain boundaries in polycrystalline silicon solar cell evalulated by laser beam induced current. *Solar Energy Materials & Solar Cells*, Vol.91, No.1, (January 2007), pp. 1-5, ISSN 0927-0248.

O'Regan, B.; Grätzel, M. (1991). A low-cost, high-efficiency solar cell based on dye-sensitized colloidal TiO_2 films. *Nature*, Vol.353, No.1 (October 1991), pp. 737-740, ISSN 0028-0836.

Peter, L.M. (2007). Characterization and modeling of dye-sensitized solar cells. *Journal of Physical Chemistry C*, Vol. 111, No.18, (April 2007), pp. 6601-6612, ISSN 1932-7447

Poce-Fatou, J.A.; Martín, J.; Alcántara, R.; Fernández-Lorenzo, C. (2002). A precision method for laser focusing on laser beam induced current experiments. *Review of Scientific Instruments*, Vol.73, No.11, (November 2002), pp. 3895-3900, ISSN 0034-6748.

Sontag, D.; Hahn, G.; Geiger, P.; Fath, P. & Bucher, E. (2002). Two-dimensional resolution of minority carrier diffusion constants in different silicon materials. *Solar Energy Materials & Solar Cells*, Vol.72, No.1-4, (April 2002), pp. 533-539, ISSN 0927-0248.

van Dyk, E.E.; Radue, C. & Gxasheka, A.R. (2007). Characterization of Cu(In,Ga)Se_2 photovoltaic modules. *Thin Solid Films*, Vol.515, No.15, (May 2007), pp. 6196-6199, ISSN 0040-6090.

Vorasayan, P.; Betts, T.R.; Tiwari, A.N. & Gottschalg, R. (2009). Multi-laser LBIC system for thin film PV module characterisation. *Solar Energy Materials & Solar Cells*, Vol.93, No.6-7, (June 2009), pp. 917-921, ISSN 0927-0248.

Vorster, F.J.; van Dyk, E.E. (2007). High saturation solar light induced current scanning of solar cells. *Review of Scientific Instruments*, Vol.78, No.1, (January 2007), pp. 013904-1-013904-7, ISSN 0034-6748.

Walker, A.B.; Peter, L.M.; Lobato, K.; Cameron, P.J. (2006). Analysis of photovoltage decay transients in dye-sensitized soar cells. *Journal of Physical Chemistry B*, Vol.110, No.50, (October 2006), pp. 25504-25507, ISSN 1520-6106.

Yagi, T.; Nishioka, K.; Uraoka, Y.; Fuyuki, T. (2004). Analysis of electrical properties of grain boundaries in silicon solar cell using laser beam induced current. *Japanese Journal of Applied Physics*, Vol.43, No.7A, (July 2004), pp. 4068-4072, ISSN 0021-4922.

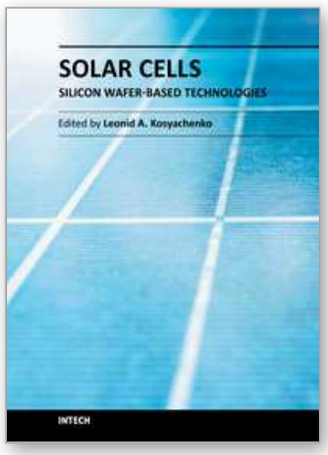

Solar Cells - Silicon Wafer-Based Technologies

Edited by Prof. Leonid A. Kosyachenko

ISBN 978-953-307-747-5
Hard cover, 364 pages
Publisher InTech
Published online 02, November, 2011
Published in print edition November, 2011

The third book of four-volume edition of 'Solar Cells' is devoted to solar cells based on silicon wafers, i.e., the main material used in today's photovoltaics. The volume includes the chapters that present new results of research aimed to improve efficiency, to reduce consumption of materials and to lower cost of wafer-based silicon solar cells as well as new methods of research and testing of the devices. Light trapping design in c-Si and mc-Si solar cells, solar-energy conversion as a function of the geometric-concentration factor, design criteria for spacecraft solar arrays are considered in several chapters. A system for the micrometric characterization of solar cells, for identifying the electrical parameters of PV solar generators, a new model for extracting the physical parameters of solar cells, LBIC method for characterization of solar cells, non-idealities in the I-V characteristic of the PV generators are discussed in other chapters of the volume.

How to reference

In order to correctly reference this scholarly work, feel free to copy and paste the following:

Javier Navas, Rodrigo Alcántara, Concha Fernández-Lorenzo and Joaquîn Martîn-Calleja (2011). Trichromatic High Resolution-LBIC: A System for the Micrometric Characterization of Solar Cells, Solar Cells - Silicon Wafer-Based Technologies, Prof. Leonid A. Kosyachenko (Ed.), ISBN: 978-953-307-747-5, InTech, Available from: http://www.intechopen.com/books/solar-cells-silicon-wafer-based-technologies/trichromatic-high-resolution-lbic-a-system-for-the-micrometric-characterization-of-solar-cells

INTECH
open science | open minds

InTech Europe
University Campus STeP Ri
Slavka Krautzeka 83/A
51000 Rijeka, Croatia
Phone: +385 (51) 770 447
Fax: +385 (51) 686 166
www.intechopen.com

InTech China
Unit 405, Office Block, Hotel Equatorial Shanghai
No.65, Yan An Road (West), Shanghai, 200040, China
中国上海市延安西路65号上海国际贵都大饭店办公楼405单元
Phone: +86-21-62489820
Fax: +86-21-62489821

IntechOpen